International Journal of Thermal Sciences 75 (2014) 204–220

Contents lists available at ScienceDirect

International Journal of Thermal Sciences

journal homepage: www.elsevier.com/locate/ijts

Investigation of nanofluid mixed convection in a shallow cavity using a two-phase mixture model

M. Goodarzi [a], M.R. Safaei [b], K. Vafai [c,*], G. Ahmadi [d], M. Dahari [b], S.N. Kazi [b], N. Jomhari [a]

[a] Department of Software Engineering, Faculty of Computer Science & Information Technology, University of Malaya, 50603 Kuala Lumpur, Malaysia
[b] Department of Mechanical Engineering, Faculty of Engineering, University of Malaya, 50603 Kuala Lumpur, Malaysia
[c] Department of Mechanical Engineering, University of California, Riverside, CA 92521, USA
[d] Department of Mechanical and Aeronautical Engineering, Clarkson University, Potsdam, NY 13699-5700, USA

ARTICLE INFO

Article history:
Received 28 April 2013
Received in revised form
7 August 2013
Accepted 8 August 2013
Available online

Keywords:
Mixed convection
Nanofluid
Mixture model

ABSTRACT

Laminar and turbulent mixed convection heat transfer of water/Cu nanofluids in a rectangular shallow cavity was studied utilizing a two-phase mixture model. The upper movable lid of the cavity was at a lower temperature compared to the bottom wall. Simulations were performed for Grashof numbers of 10^5 (laminar flow) and 10^{10} (turbulent flow) for Richardson numbers from 0.03 to 30, and nanoparticle volume fractions of 0.00–0.04. The two-dimensional governing equations were discretized using a finite volume method. The effects of nanoparticle concentration, shear and buoyancy forces, and turbulence on flow and thermal behavior of nanofluid flow were studied. The model predictions for very low solid volume fraction ($\varphi \approx 0$) were found to be in good agreement with earlier numerical studies for a base fluid. It is shown that for specific Grashof (*Gr*) and Richardson (*Ri*) numbers, increasing the volume fraction of nanoparticles enhances the convective heat transfer coefficient and consequently the Nusselt number (*Nu*) while having a negligible effect on the wall shear stress and the corresponding skin friction factor.

1. Introduction

Advances in nanofluids acting as a new heat transfer medium have introduced new and exciting potentials. The common working fluids used in industries such as water, ethylene glycol and oil typically have lower thermal conductivity compared to metals and metal oxides. By adding high-conductivity solid materials to base fluids it is possible to enhance the mixture's heat transfer performance. The notion of adding micro-sized solid materials to base fluids was proposed decades ago. However, because micro-particles have the tendency to settle in the suspension, it can result in potential adverse effect. Additional problems could be that micro-sized abrasive solid materials erode and corrode pipes and damage pumps or other devices. Nanofluids comprised of nano-sized particles suspended in base fluids could mitigate the issues of erosion, corrosion, fouling and blocking. An increase in thermal conductivity without causing a major pressure drop is a principal advantage of nanofluids. As a result, the performance of numerous heat transfer devices can be augmented, directly leading to the higher capacity of operating units. Nanofluids are also utilized in electronic cooling applications [1].

The practical application of mixed convection heat transfer in various areas such as solar collectors, double-layer glass, building insulation, electronic cooling, food drying, and sterilization among others, has been reported in literature. Mixed convection heat transfer occurs in several ways. One way is to move the walls within a cavity in the presence of hot or cold fluid. Shear stresses are thus produced, forming hydrodynamic and thermal boundary layers in the enclosed fluid, eventually leading to a forced convection condition. Numerous studies have been conducted in this area. Among the notable works are those by Khanafer and Vafai [2], Chung and Vafai [3] and Sharif [4]. Another technique is to introduce hot or cold fluid from one side through the isothermal walls, and have the fluid exit from the other side. A number of researchers have imposed a constant heat flux on the wall as the fluid passes through the channel, and subsequently analyzed the heat transfer effect [5–9].

In recent years studies on nanofluid flow and heat transfer in cavities and enclosures have attracted considerable attention. The majority of studies focus on the laminar flow regime. Muthtamilselvan et al. [10] employed a finite volume method to examine the mixed convection heat transfer of Cu/water nanofluid in a lid-driven rectangular cavity. Two of the cavity's vertical walls were

* Corresponding author. Tel.: +1 951 827 3125; fax: +1 951 827 2899.
E-mail address: vafai@engr.ucr.edu (K. Vafai).

1290-0729/$ – see front matter
http://dx.doi.org/10.1016/j.ijthermalsci.2013.08.003

Nomenclature

AR	aspect ratio
K_b	Boltzmann constant (1.3807×10^{-23} J K^{-1})
x,y	Cartesian coordinates (m)
H	cavityheight (m)
Cu	copper
d_f	diameter of the base fluid molecule (m)
d_p	diameter of nanoparticle molecule (m)
Y^+	dimensionless distance from the wall
U^+	dimensionless velocity
Y_p	distance from the wall-adjacent cell to the wall (m)
f_{drag}	drag function
Gr	Grashof Number ($g\beta_m \Delta T W^3\ \upsilon_m^{-2}$)
$\vec{g}$	gravitational acceleration (m s^{-2})
h	heat transfer coefficient (W m^{-2} K^{-1})
$\bar{u}$	mean velocity (m s^{-1})
n	number of phases
Nu	Nusselt Number ($h_m W k_m^{-1}$)
Pr	Prandtl Number ($\upsilon_m \alpha_m^{-1}$)
P	pressure (N m^{-2})
Ra	Rayleigh Number ($Gr\ Pr$)
V_{pf}	relative velocity (slip velocity) (m s^{-1})
Re	Reynolds Number ($V_m W \upsilon_m^{-1}$)
Ri	Richardson Number ($Gr\ Re^{-2}$)
$\vec{a}$	Secondary-phase (Particle) acceleration (m s^{-2})
h_k	sensible enthalpy for phase k (J kg^{-1})
C_p	specific heat capacity (J kg^{-1} K^{-1})
T	Temperature (K)
t	time (s)
Y	the local coordinate normal to the wall
k	thermal conductivity (W m^{-1} K^{-1})
K	turbulent kinetic energy (m^2 s^{-2})
K_p	turbulence kinetic energy at the wall-adjacent cell (m^2 s^{-2})
K_t	turbulent thermal conductivity (W m^{-1} K^{-1})
u,v	velocities components in X and Y directions (m s^{-1})
$\dot{q}$	wall heat flux (W m^{-2})
W	Width of the cavity (m)

Greek symbols

ρ	density (kg m^{-3})
ε	dissipation rate of turbulent kinetic energy (m^2 s^{-3})
μ	dynamic viscosity (Pa S)
υ	kinematics viscosity (m^2 s^{-1})
σ_D	Prandtl dispersion coefficient
α_m	thermal diffusivity ($\mu_m \rho_m^{-1}$)
β	thermal expansion coefficient (K^{-1})
$\upsilon_{t,m}$	turbulent Eddy viscosity (m^2 s^{-1})
σ_T	turbulent thermal diffusivity (m^2 s^{-1})
ϕ	volume fraction of nanoparticles
τ_w	wall shear stress (Pa)

Subscripts

f	base fluid
c	cold wall
Dr	drift
eff	effective
h	wall
Z	indices
0	inlet conditions
lid	lid
M	mean
m	mixture
np	nanoparticles
P	point P
W	point W
F	primary phase
rms	root mean square
p	secondary phase
T	thermal
t	turbulent
W	wall

insulated; the bottom horizontal wall's temperature was maintained at T_c while the temperature of the top moving wall was T_h. Their results show that solid volume fraction and aspect ratio affect heat transfer and fluid flow within the cavity. Also they found that the average Nusselt number varies linearly with respect to solid volume fraction.

Abu-Nada and Chamkha [11] investigated the steady natural convection of CuO–EG–water nanofluid inside a rectangular enclosure using a finite volume method. In their study, the Rayleigh number varied from 10^3 to 10^5, the nanoparticle volume fraction varied from 0% to 6%, and the aspect ratio varied from 0.5 to 2. Flow streamlines and temperature contours were evaluated along with the average and local Nusselt numbers. They found that at low aspect ratios (AR), the average Nusselt number improved with an increase in nanoparticle volume fraction.

Karimipour et al. [12] recently studied the periodic mixed convection of copper/water nanofluid in a rectangular cavity with AR = 3. The examined cavity had two vertical adiabatic walls. The temperature of the upper wall that oscillated at a speed of $U = U_0 \times \sin(\omega t)$ was less than the lower wall's temperature. They demonstrated that due to the oscillating wall, heat transfer improved in the cavity. Khanafer et al. [13] investigated the unsteady mixed convection of air in a sinusoidal lid-sliding cavity utilizing finite element method. Their study indicated that the Grashof and Reynolds numbers had a significant impact on the nature and structure of flow in the cavity.

Oztop and Abu-Nada [14] analyzed the natural convection for different nanofluids in a partially heated square enclosure. They studied a wide range of Rayleigh numbers ($10^3 \leq Ra \leq 5 \times 10^5$), heater heights, heater locations, aspect ratios and solid volume fractions. As expected they found that an increase in heater size and Rayleigh number led to better heat transfer and fluid flow throughout the cavity. In addition, they found that the nanofluid is a key factor in heat transfer performance. They reported that the copper/water nanofluid had the highest heat transfer rate among the investigated cases.

Ghasemi and Aminossadati [15] used a finite volume method to assess the free convection in an inclined square enclosure with two insulated vertical walls and two horizontal walls at different temperatures. Pure water and CuO–water with $0.01 \leq \Phi \leq 0.04$ were used in their study. The Rayleigh number varied between 10^3 and 10^7 and the inclination angle ranged between 0 and 90° to examine the impact of these factors on heat transfer and fluid flow in the enclosure. They found that at low Rayleigh numbers where heat transfer occurs mainly by conduction, the flow patterns and temperature contours are similar at 30–90-degree inclination angles. However, for Rayleigh numbers above 10^5, the temperature and flow patterns at a 0-degree inclination angle are different from the other inclination angles. Ravnik et al. [16] investigated the 3D natural convection flow using the boundary elements method. Air and pure water served as the simple base fluids, while TiO_2, Al_2O_3 and Cu nanoparticles suspended in water acted as nanofluids. It was demonstrated that utilizing nanofluids, the largest heat transfer enhancements occurs in the conduction dominated regime.

Despite a lot of progress in computing power and experimental techniques, the analysis of turbulent flows inside a cavity remains a challenging topic in fluid mechanics. It is also rather difficult to measure flow velocities at low speeds in enclosed boundary layers with the presently available sensors and probes. Even with progress in numerical methods such as DES, LES, and DNS, it is still difficult to predict stratification in the core of a cavity.

The literature review indicates a lack of comprehensive studies in turbulent mixed convection heat transfer of nanofluids inside cavities. Most research works concern turbulent forced convection or natural convection heat transfer inside tubes. For example, using a numerical method and a single-phase model, Maiga et al. [17,18] studied the laminar and turbulent forced convection heat transfer of ethylene glycol–γAl_2O_3 and water/γAl_2O_3 nanofluids in a heated tube 1 m long. The results demonstrated that the ethylene glycol–γAl_2O_3 transfers more heat than the water/γAl_2O_3. However, in another article, Maiga et al. [19] reported the negative forced convection performance of nanofluids in a tube. The nanofluids also increased the walls' shear stresses, hence raising the pumping cost.

In a more recent study, Bianco et al. [20] examined the turbulent forced convection heat transfer of water/Al_2O_3 nanofluids inside a 1 m-long tube with a diameter of 0.01 m, utilizing the two-phase mixture model in FLUENT software. The aluminum oxide particles had a 38 nm diameter. As expected, the highest heat transfer rate for a given concentration was achieved at the largest Reynolds number while the increase in particle volume fraction amplified the heat transfer.

Nguyen et al. [21] experimentally studied the heat transfer and erosion/corrosion of the water/Al_2O_3 nanofluid with $\Phi = 5\%$ for an impinging jet system. Their study showed that the surface heat transfer coefficient improves significantly, but their erosion tests demonstrated that nanofluids have the potential to cause premature wear of mechanical systems.

The presented literature survey suggests that nanofluids are an effective coolant [22–24] but their possible corrosive nature [21] requires additional investigations. In particular, the natural and mixed convection heat transfer of nanofluids in a turbulent flow regime is still not entirely understood. In the present study, laminar and turbulent mixed convection heat transfer of dilute water/Cu nanofluids in a cavity with an aspect-ratio of AR = 0.1 is analyzed. FLUENT software was used for the analysis. The formulas for nanofluid properties and the top moving lid boundary condition were introduced into the software via User Defined Functions (UDFs). The RNG k–ε turbulence model was used for turbulent flow analysis. The flow regime's simulation results were weighed against model validation results found in the literature. Particular attention was paid to the laminar as well as turbulent mixed convection of water/Cu nanofluids with different solid volume fractions using the two-phase mixture model. The results from the present study may find applications for use as coolant fluids in solar collectors and electronic devices [24].

2. Governing equations for laminar and turbulent nanofluids

Continuum theories for multiphase mixtures were developed by Truesdell and Toupin [25], Eringen and Igram [26] and as of late, Drumheller and Bedford [27] along with Ahmadi [28,29]. A thermodynamic formulation of mixture flows in a turbulent state was developed by Ahmadi and Ma [30], Abu-Zaid and Ahmadi [31], and Ahmadi et al. [32]. Applying the mixture theory for modeling nanofluids was described by Shariat et al. [33] and Alikhani et al. [34]. In this approach, a single fluid multiphase model was used in the analysis. The underlying physical assumption is that the fluid flow carries the nanoparticles. Therefore, the governing equations for the mixture's continuity, momentum, energy and turbulence are employed for flow analysis. Mixture density is computed by invoking the Boussinesq approximation for $\Delta T < 30$ °C. It is assumed the nanoparticles are spherical with a diameter of 10 nm and move at the same mean velocity as that of the base fluid, while other properties are assumed to be constant. The governing equations are [33–41]:

Continuity Equation:

$$\frac{\partial}{\partial t}(\rho_{\rm m}) + \nabla\cdot(\rho_{\rm m}\vec{V}_{\rm m}) = 0 \tag{1}$$

where

$$\vec{V}_{\rm m} = \frac{\sum_{Z=1}^{n}\phi_Z\rho_Z\vec{V}_Z}{\rho_{\rm m}} = \vec{V}_Z \tag{2}$$

and

$$\rho_{\rm m} = \sum_{Z=1}^{n}\phi_Z\rho_Z \tag{3}$$

Momentum Equation:

$$\frac{\partial}{\partial t}(\rho_{\rm m}\vec{V}_{\rm m}) + \nabla\cdot(\rho_{\rm m}\vec{V}_{\rm m}\vec{V}_{\rm m}) = -\nabla P_{\rm m} + \nabla\cdot\left[\mu_{\rm m}\left(\nabla\vec{V}_{\rm m} + \nabla\vec{V}_{\rm m}^{T}\right)\right] + \rho_{\rm m}\beta_{\rm m}(T - T_0)g \tag{4}$$

where

$$\mu_{\rm m} = \sum_{Z=1}^{n}\phi_Z\mu_Z \tag{5}$$

and

$$\vec{V}_{dr,Z} = \vec{V}_Z - \vec{V}_{\rm m} = 0 \tag{6}$$

Energy Equation:

$$\frac{\partial}{\partial t}\rho_{\rm m}h_{\rm m} + \nabla\cdot(\rho_{\rm m}h_{\rm m}\vec{V}_{\rm m}) + \nabla\cdot(P\vec{V}_{\rm m}) = \nabla\cdot\left(K_{\rm eff}\nabla T\right) \tag{7}$$

where

$$\rho_{\rm m}h_{\rm m} = \sum_{Z=1}^{n}(\varphi_Z\rho_Z h_Z) \tag{8}$$

and

$$k_{\rm eff} = \sum_{Z=1}^{n}\varphi_Z(K_Z + K_{\rm t}) \tag{9}$$

RNG k–ε turbulence model:

Turbulent kinetic energy transport equation:

Table 1
Coefficients for RNG $k-\varepsilon$ turbulent model [47].

C_μ	σ_k	σ_ε	C_1	C_2	η_0	β	K
0.0845	1	1.3	1.42	1.68	4.38	0.012	0.41

$$\frac{\partial K}{\partial t}+\vec{u}_m\frac{\partial K}{\partial x}+\vec{v}_m\frac{\partial K}{\partial y}=\frac{\partial}{\partial x}\left(\upsilon_m+\frac{\upsilon_{t,m}}{\sigma_k}\right)\frac{\partial K}{\partial x}+\frac{\partial}{\partial y}\left(\upsilon_m+\frac{\upsilon_{t,m}}{\sigma_k}\right)\frac{\partial K}{\partial y}+P_{k,m}+G_{k,m}-\varepsilon \tag{10}$$

Dissipation of turbulent kinetic energy transport equation:

$$\frac{\partial \varepsilon}{\partial t}+\vec{u}_m\frac{\partial \varepsilon}{\partial x}+\vec{v}_m\frac{\partial \varepsilon}{\partial y}=\frac{\partial}{\partial x}\left(\upsilon_m+\frac{\upsilon_{t,m}}{\sigma_\varepsilon}\right)\frac{\partial \varepsilon}{\partial x}+\frac{\partial}{\partial y}\left(\upsilon_m+\frac{\upsilon_{t,m}}{\sigma_\varepsilon}\right)\frac{\partial \varepsilon}{\partial y}+C_1\frac{\varepsilon}{K}P_{k,m}+C_2\frac{\varepsilon^2}{K}+C_3\frac{\varepsilon}{K}G_{k,m}-R_{\varepsilon,m} \tag{11}$$

The eddy viscosity obtained from Prandtl–Kolomogorov relation:

$$\upsilon_{t,m}=C_\mu f_\mu\frac{K^2}{\varepsilon} \tag{12}$$

The turbulence kinetic energy production term, P_k, is given as:

$$P_{K,m}=\upsilon_{t,m}\left[2\left(\frac{\partial \vec{u}_m}{\partial x}\right)^2+2\left(\frac{\partial \vec{v}_m}{\partial x}\right)^2+\left(\frac{\partial \vec{u}_m}{\partial y}+\frac{\partial \vec{v}_m}{\partial y}\right)^2\right] \tag{13}$$

The buoyancy term, G_k, is defined by:

$$G_{K,m}=-g\beta\frac{\upsilon_{t,m}}{\sigma_t}\frac{\partial T}{\partial y} \tag{14}$$

The $R_{\varepsilon,m}$ term in RNG $k-\varepsilon$ model, is given as:

$$R_{\varepsilon,m}=\frac{C_{\mu,m}\rho_m\eta^3\left(1-\frac{\eta}{\eta_0}\right)}{1+\beta\eta^3}\frac{\varepsilon^2}{K} \tag{15}$$

where:

$$\eta=\frac{SK}{\varepsilon} \tag{16}$$

The constant C_3, can be expressed as:

$$C_3=\tan\left|\frac{\vec{v}_m}{\vec{u}_m}\right| \tag{17}$$

The main difference between the standard $k-\varepsilon$ and RNG $k-\varepsilon$ method lies in the ε equation, in which the analytical formulas for turbulent Prandtl numbers are improved. [43–46].

The constants for the RNG $k-\varepsilon$ turbulence model in the above relations are presented in Table 1 [47].

The local Nusselt number along the upper and bottom walls and the average Nusselt number can be calculated respectively as [4,12]:

$$Nu_h=-\frac{k_m}{k_f}\left(\frac{\partial T}{\partial Y}\right)_{Y=0} \tag{18}$$

$$Nu_c=-\frac{k_m}{k_f}\left(\frac{\partial T}{\partial Y}\right)_{Y=1} \tag{19}$$

Table 2
Thermophysical properties of the base fluid and Cu nanoparticles [48].

	Copper (Cu)	Water
ρ (kg m^{-3})	8933	997.1
k (W m^{-1} K^{-1})	400	0.613
C_p (J kg^{-1} K^{-1})	385	4179
β (K^{-1})	0.0000167	0.00021
μ (Pa s)	–	0.000891

$$Nu_M=\frac{1}{W}\int_0^W Nu_x\,dx \tag{20}$$

2.1. Nanofluid properties

The thermophysical properties of water (as base fluid) and copper (as nanoparticles) are provided in Table 2. The nanofluid properties can be obtained from the base fluid and nanoparticles' properties. Nanofluid density and heat capacity are evaluated based on the recommendations of Ramiar et al. [49] and Khanafer and Vafai [50].

$$\rho_m=\varphi\rho_{np}+(1-\varphi)\rho_f \tag{21}$$

$$(\rho c_p)_m=(1-\varphi)(\rho c_p)_f+\varphi(\rho c_p)_{np} \tag{22}$$

With respect to thermal conductivity, Chon et al. [51] presented a model which includes the effects of temperature, Brownian motion and sub-layer thickness [52]:

$$\frac{k_m}{k_f}=1+64.7\ \varphi^{0.746}\left(\frac{d_f}{d_{np}}\right)^{0.369}\left(\frac{k_{np}}{k_f}\right)^{0.7476}\Pr^{0.9955}\mathrm{Re}^{1.2321} \tag{23}$$

where $Pr=\mu_f/\rho_f\alpha_f$ and $\mathrm{Re}=\rho_f k_b T/3\pi\mu^2 l_f$ are the Prandtl and Brownian Reynolds numbers, l_f the base fluid's mean free path (0.17 nm for water) and μ is the temperature-dependent viscosity of the base fluid expressed as:

$$\mu=O\times 10^{\frac{P}{T-Q}} \tag{24}$$

where O, P, and Q are constants. For water they are equal to 2.414×10^{-5}, 247.8 and 140 respectively [52].

Masoumi et al. [53] suggested a new model for dynamic nanofluid viscosity that comprises the effects of temperature, mean diameter of nanoparticles, volume fraction of nanofluid, density of nanoparticles and the thermophysical properties of the base fluid [33,49] as:

$$\frac{\mu_m}{\mu_f}=1+\frac{\rho_{np}V_B d_{np}^2}{72Q\delta} \tag{25}$$

where $\delta=\sqrt[3]{(\pi/6\varphi)}d_{np}$ is the mean distance between the nanoparticles' centers and $V_B=1/d_{np}\sqrt{18\,k_bT/\pi\rho_{np}d_{np}}$ is the Brownian velocity of nanoparticles. In Equation (25), $Q=(c_1\varphi+c_2)d_{np}+(c_3\varphi+c_4)$ is the fitting parameter. The constants are evaluated form the experimental data and are given as: $c_1=-1.133\ e^{-6}$, $c_2=-2.771\ e^{-6}$, $c_3=9.0\ e^{-8}$ and $c_1=-3.93\ e^{-7}$ [49].

The coefficient of thermal expansion can be computed from the expression suggested by Khanafer et al. [54] and Abouali and Ahmadi [55]:

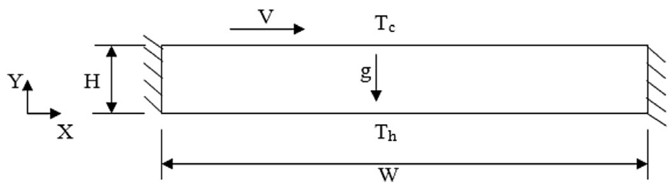

Fig. 1. Schematic of analyzed configuration.

$$\beta_m = \beta_f \left[\frac{1}{1+\frac{(1-\phi)\rho_f}{\phi\rho_{np}}} \frac{\beta_{np}}{\beta_f} + \frac{1}{1+\frac{\phi\rho_{np}}{(1-\phi)\rho_f}} \right] \tag{26}$$

3. Boundary conditions

A schematic of the configuration analyzed in the present study along with the boundary conditions is shown in Fig. 1. The cavity's aspect ratio is AR = H/W and AR = 0.1 is the default value used in the simulations unless otherwise specified.

The specific boundary conditions for the present study are:

$$\begin{aligned}
&\frac{\partial T}{\partial y} = 0 \quad && u = v = 0 \quad && 0 < y < 1 \quad && x = 0\\
&\frac{\partial T}{\partial y} = 0 \quad && u = v = 0 \quad && 0 < y < 1 \quad && x = 10\\
&T = T_h \quad && u = v = 0 \quad && 0 < x < 10 \quad && y = 0\\
&T = T_c \quad && v = 0,\ u = u_{lid} \quad && 0 < x < 10 \quad && y = 1
\end{aligned} \tag{27}$$

3.1. Wall function modeling

The standard wall function was described by Launder and Spalding [56] and is used in Abedini et al. [57] as a semi-empirical formula based on the established properties of turbulence in the inertial sub-layer near a wall. In this approach, the velocity at the first grid is given as:

$$U^+ = 2.389\ \ln\left(9.793Y^+\right) \tag{28}$$

where

$$\begin{aligned}
U^+ &= \frac{U_P C_\mu^{0.25} K_P^{0.5}}{\tau_w/\rho}\\
y^+ &= \frac{\rho Y_P C_\mu^{0.25} K_P^{0.5}}{\mu}
\end{aligned} \tag{29}$$

The logarithmic law for the mean velocity is valid for the range $11 \le y^+ \le 300$. When the meshes are in such a way that $y^+ \le 11$ at the wall-adjacent cells, in the viscous sub-layer, the linear velocity profile holds. That is,

$$U^+ = Y^+$$

For the temperature boundary conditions:

$$\begin{aligned}
T^+ &= \frac{\rho C_P (T_W - T_P) C_\mu^{0.25} K_P^{0.5}}{\dot{q}}\\
&= \begin{cases} \Pr Y^+ & \left(Y^+ < Y_T^+\right)\\ 0.85\left[2.389\ln(9.793Y^+) + \zeta\right] & \left(Y^+ > Y_T^+\right) \end{cases}
\end{aligned} \tag{30}$$

where

$$\zeta = 9.24\left[\left(\frac{\Pr}{0.85}\right)^{0.75} - 1\right]\left[1 + 0.28e^{-0.007\Pr/0.85}\right] \tag{31}$$

For the turbulence $K-\varepsilon$ model:

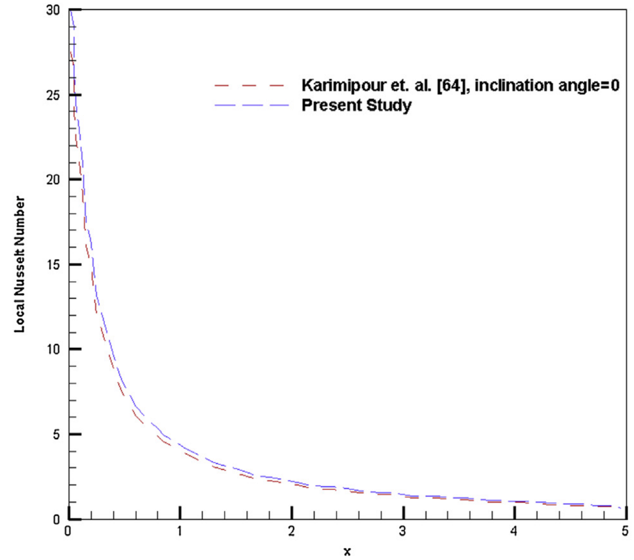

a) Ri =1, comparison with the work of Karimipour et al. [64] for hot wall

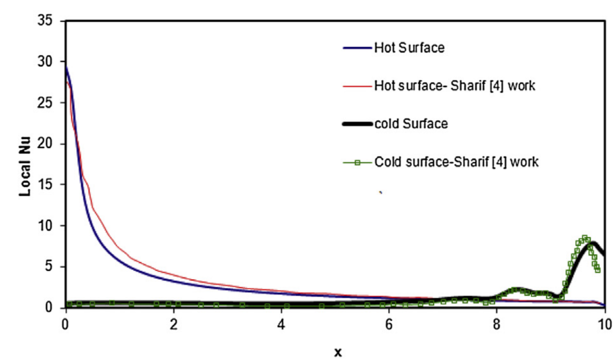

b) Ri =1, comparison with the work of Sharif [4] for both hot and cold walls

Fig. 2. Comparison of the local Nusselt number variations with previous works, laminar mixed convection regime.

The boundary conditions for turbulent kinetic energy is given as

$$\frac{\partial K}{\partial Y} = 0 \tag{32}$$

The corresponding turbulence kinetic energy production term is given by:

$$P_k \approx \tau_w \frac{\partial u}{\partial y} = \tau_w \frac{\tau_w}{0.4187 \rho C_\mu^{0.25} Y_p K_P^{0.5}} \tag{33}$$

At the wall-adjacent cells, the ε equation is not solved. But instead ε_P is evaluated as [57]:

$$\varepsilon_P = \frac{C_\mu^{0.75} K_p^{1.5}}{k Y_p} \tag{34}$$

4. Numerical method

In order to solve the partial differential equations that govern nanofluid flow, the FLUENT commercial code – based on the finite volume method – was used. The finite volume method is a specific case of the weighting residual method, where the computational field is divided into finite control volumes as each node

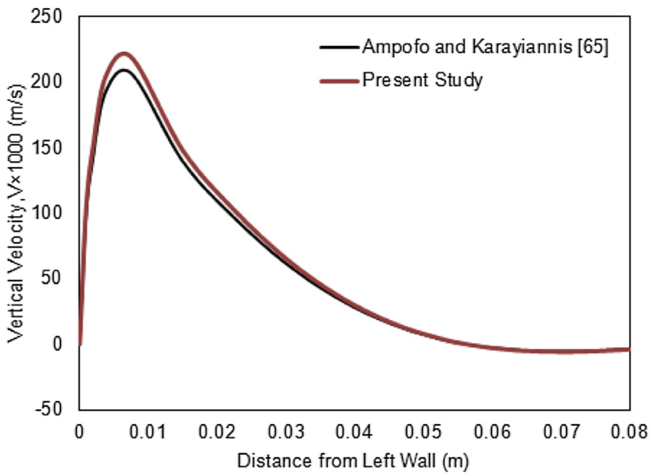

Fig. 3. Boundary layer structure of vertical velocity profile along the hot wall, $y/H = 0.5$, comparison with the work of Ampofo and Karayiannis [65].

corresponds to a control volume. The differential equation is subsequently integrated over each finite volume [57–61]. The second-order upwind method was employed for the discretization of the convective and diffusive terms, while the SIMPLEC procedure [58,62,63] was selected for pressure–velocity coupling. The calculation concluded when the residuals for all equations dropped below 10^{-7}.

5. Numerical procedure validation

The validation of the present numerical solution is discussed in this section. The simulation results are compared with the available results from the literature. For this purpose, the limiting case of a negligible amount of nanoparticles ($\varphi = 0.00001$) was used. Simulation results were found to be similar to those for pure liquid as can be seen in Figs. 2 and 4. It was concluded that the numerical method is highly reliable and accurate and can be used to predict mixed convection heat transfer in a shallow rectangular cavity.

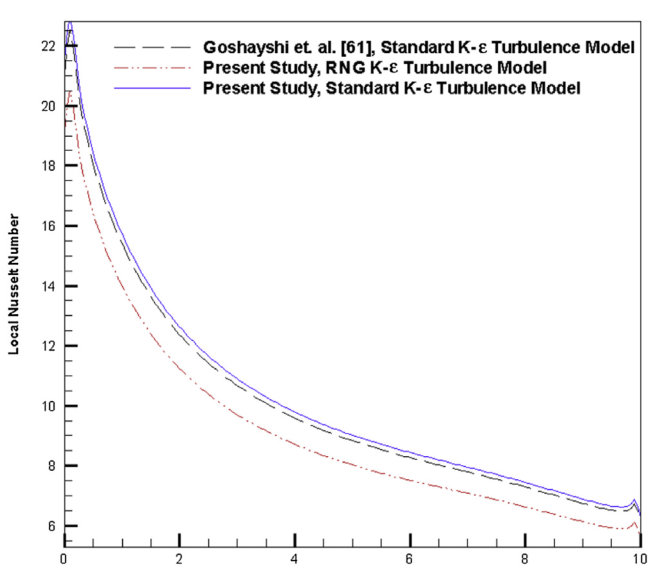

Fig. 4. Comparison of the local Nusselt number variations along the hot wall for $Ri = 0.1$ and $Ra = 10^9$ with the work of Goshayshi et al. [61].

Table 3
Details of Ampofo and karayiannis's study [65].

Rayleigh number	1.58×10^9
Length of cavity (m)	0.75
Wide of cavity (m)	0.75
Left wall temperature (°C)	50
Right wall temperature (°C)	10
Prandtl number	0.707

Table 4
Comparison of the local Nusselt number variations along top and bottom walls, with the work of Ampofo and Karayiannis [65].

X/L	Ampofo and Karayiannis [65]		Present study	
	Nu (bottom wall)	Nu (top wall)	Nu (bottom wall)	Nu (top wall)
0.0133	75.0000	22.0000	75.0180	22.0080
0.0400	58.0000	18.0000	58.0230	18.0140
0.0800	40.0000	8.0000	40.0280	8.0190
0.1333	38.0000	5.0000	38.0330	5.0220
0.2000	36.0000	2.0000	36.0370	2.0250
0.2800	20.0000	−4.0000	20.0350	−3.9310
0.3600	16.0000	−8.0000	16.0310	−7.9190
0.5000	10.0000	−11.0000	10.0260	−10.8890
0.6400	8.0000	−18.0000	8.0220	−17.9360
0.7200	4.0000	−23.0000	4.0170	−22.9630
0.8000	1.0000	−31.0000	1.0120	−30.9710
0.8667	−12.0000	−35.0000	−11.9190	−34.9750
0.9200	−15.0000	−42.0000	−14.9310	−41.9780
0.9600	−19.0000	−55.0000	−18.9660	−54.9820
0.9867	−25.0000	−70.0000	−24.9720	−69.9880

5.1. Laminar mixed convection validation

With the intention of validating the laminar mixed convection, the results from this work were contrasted against those obtained by Karimipour et al. [64] and Sharif [4]. These researchers had investigated laminar mixed convection heat transfer of water in a shallow lid-driven cavity with an aspect ratio of 0.2 [64] and 0.1 [4] that was cooled from the bottom and heated from the top movable wall. To compare with their work, calculations were performed for $0.001 \le Ri \le 100$ [64] and $0.1 \le Ri \le 10$ [4], and the Reynolds number remained fixed at $Re = 408.21$. The computed Nusselt number was compared with the work of Karimipour et al. [64] and Sharif [4], as shown in Fig. 2a and b which demonstrates an excellent agreement between the present simulation results with those of these researchers.

5.2. Turbulent natural convection validation

Ampofo and Karayiannis [65] have reported an experimental study on turbulent natural convection of air inside a square cavity which is used as a benchmark data for validation of numerical models. Peng and Davidson [66] studied the same flow using the LES, Omri and Galanis [67] used the SST k–ω and Hsieh and Lien [68] used steady RANS Low-Re k–ε model and analyzed this flow.

Table 5
Grid independence tests for the laminar regime.

Number of grids	50 × 5	100 × 10	200 × 20
Average Nusselt number at the hot wall for $Ri = 0.03$	11.8452	14.29078	14.4521
Average Nusselt number at the hot wall for $Ri = 1$	3.2145	4.91902	4.9878
Average Nusselt number at the hot wall for $Ri = 30$	4.0021	4.23035	4.2706

Table 6
Grid independence tests for the turbulence RNG $k-\varepsilon$ model.

Number of grids (Ri = 0.03)	**610 × 61**	**1190 × 119**	**1810 × 181**
Average Nusselt number at the hot wall for $Ri = 0.03$	79.9632	83.4906	84.8087
Number of grids (Ri = 1)	**810 × 81**	**1600 × 160**	**2410 × 241**
Average Nusselt number at the hot wall for $Ri = 1$	73.0002	76.41512	78.2130
Number of grids (Ri = 30)	**900 × 90**	**1750 × 175**	**2700 × 270**
Average Nusselt number at the hot wall for $Ri = 30$	45.8736	49.38171	50.9201

To validate the present numerical method, the problem, which was studied by Ampofo and Karayiannis [65], is simulated using the RNG $k-\varepsilon$ turbulence model. The details of the computed Nusselt number for the top and bottom walls and comparison with the data of Ampofo and Karayiannis [65], respectively, are shown in Tables 3 and 4. The vertical velocity profile near the hot wall, at mid-height of cavity which shows the features of a natural convection boundary layer is illustrated in Fig. 3. These results show that the present model simulations are in good agreement with the experimental benchmark data.

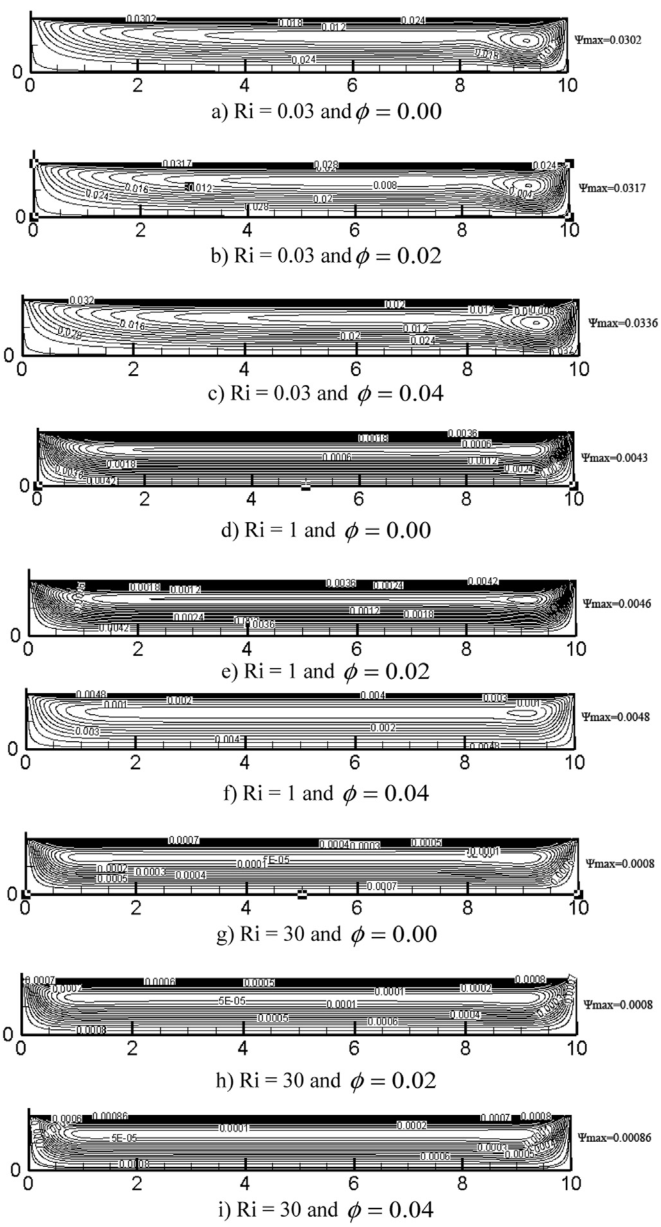

Fig. 5. Streamlines for laminar flow regime.

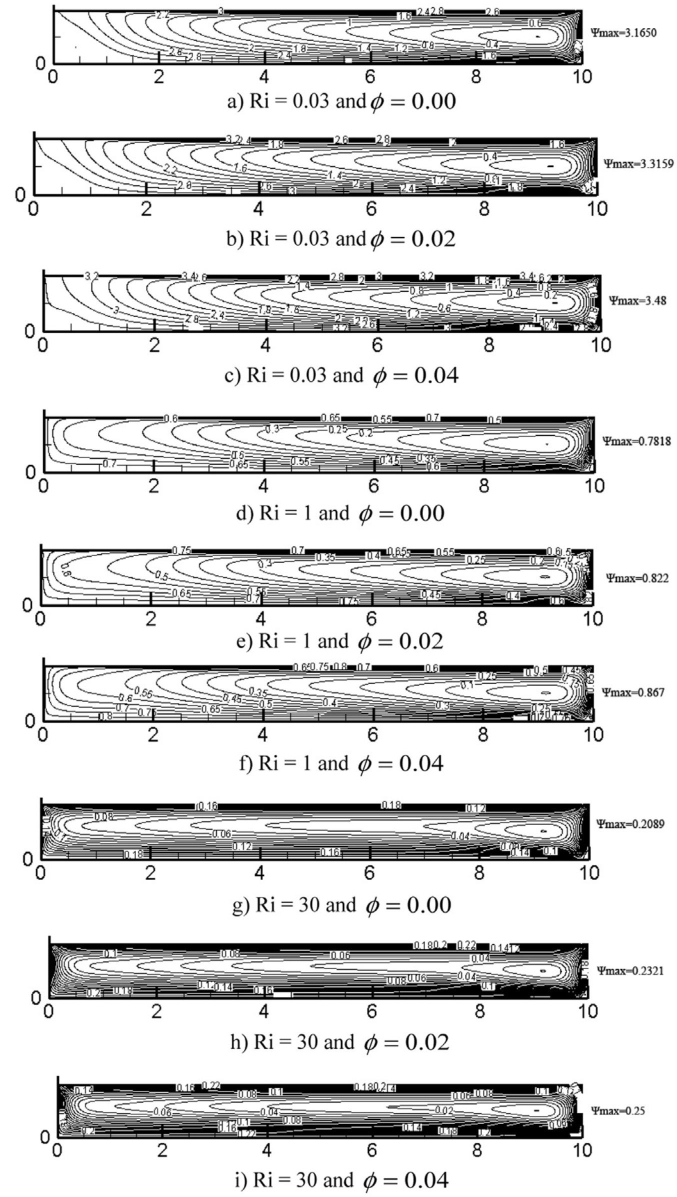

Fig. 6. Mean flow streamlines for turbulent flow regime.

5.3. Turbulent mixed convection validation

The current numerical procedure for solving turbulent mixed convection was further compared with the results of Goshayshi et al.'s [61] study on enclosed turbulent mixed convection. In that work, laminar and turbulent mixed convection heat transfer of water in a shallow lid-driven cavity with an aspect ratio of 0.1, cooled from the bottom and heated from the top movable wall, was evaluated numerically using finite volume method. Calculations were done for$0.01 \leq Ri \leq 100$. The Ra was varied from 10^5 to 10^7 for laminar flow and 10^9 to 10^{11} for turbulent flow, but to compare with their work, the Reynolds number remained fixed at 408.21 for laminar flow and 40,821 for turbulent flow.

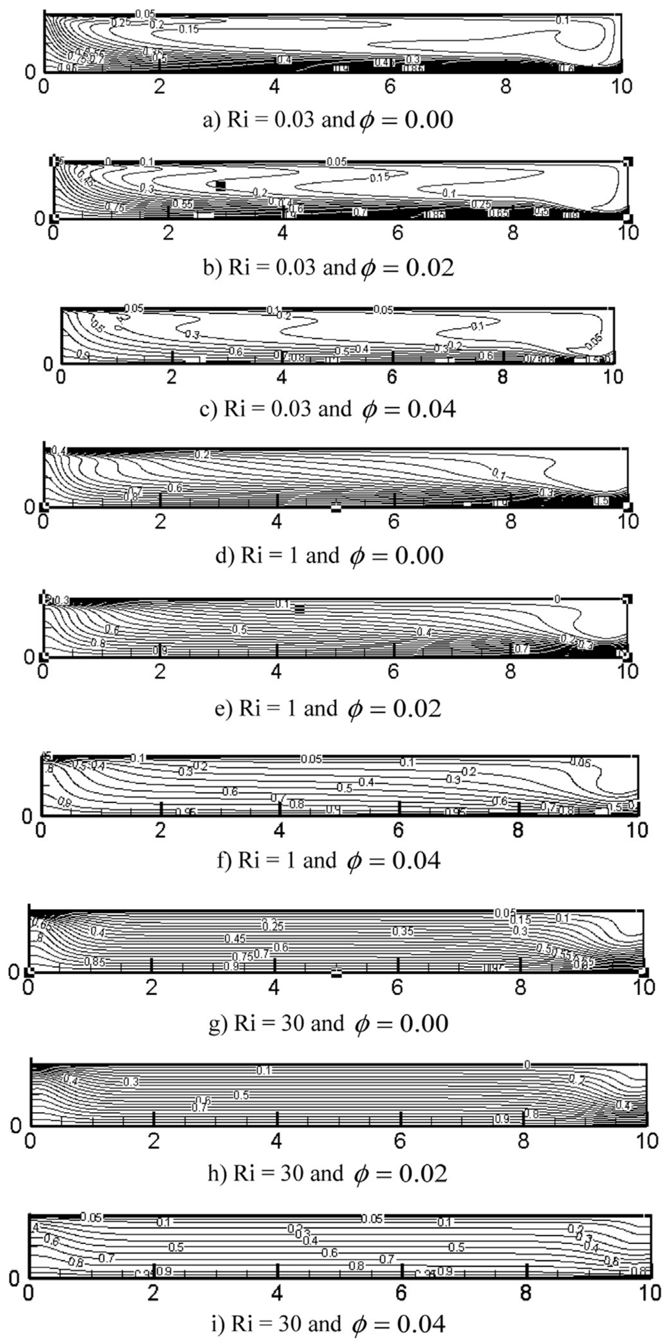

Fig. 7. Isotherms for laminar flow regime.

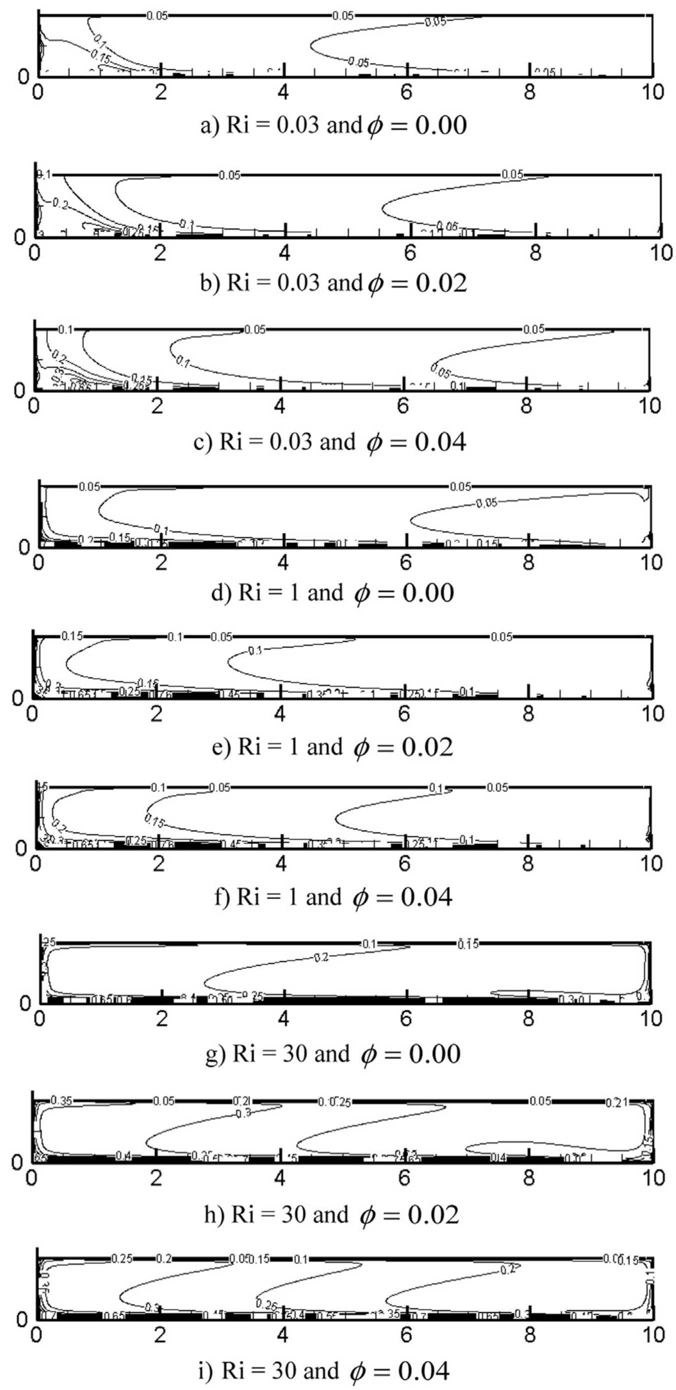

Fig. 8. Mean isotherms for turbulent flow regime.

For $Ri = 0.1$ and $Ra = 10^9$ the computed turbulence Nusselt number by Standard $k-\varepsilon$ and RNG $k-\varepsilon$ turbulence models is plotted in Fig. 4 and contrasted with the results in Ref. [61]. This figure illustrates a superior adaptation between the present simulation results using Standard $k-\varepsilon$ turbulence model with those of Goshayshi et al. [61] work. The small discrepancies observed in this figure between the present work using RNG $k-\varepsilon$ turbulence model and Goshayshi et al. [61] work are due to the differences between the employed turbulence models. However, previous research works demonstrates higher accuracy for RNG $k-\varepsilon$ turbulence model in comparison with the standard $k-\varepsilon$ turbulence model [69,70], especially in transition flows [71,72], swirl flows [73,74], rapidly strained flows [75–77] and flow around a curvature [78].

5.4. Grid independence

The computational domain was discretized via structured, non-uniform grid distributions. The grid distribution is more refined in the vicinity of walls with significant temperature and velocity gradients. Several grid distributions were tested to assure that the computational results are grid-independent. The grid independence for each turbulence model and *Ri* was studied separately. Tables 5 and 6 illustrate the result of the grid independence studies for $\Phi = 0.02$.

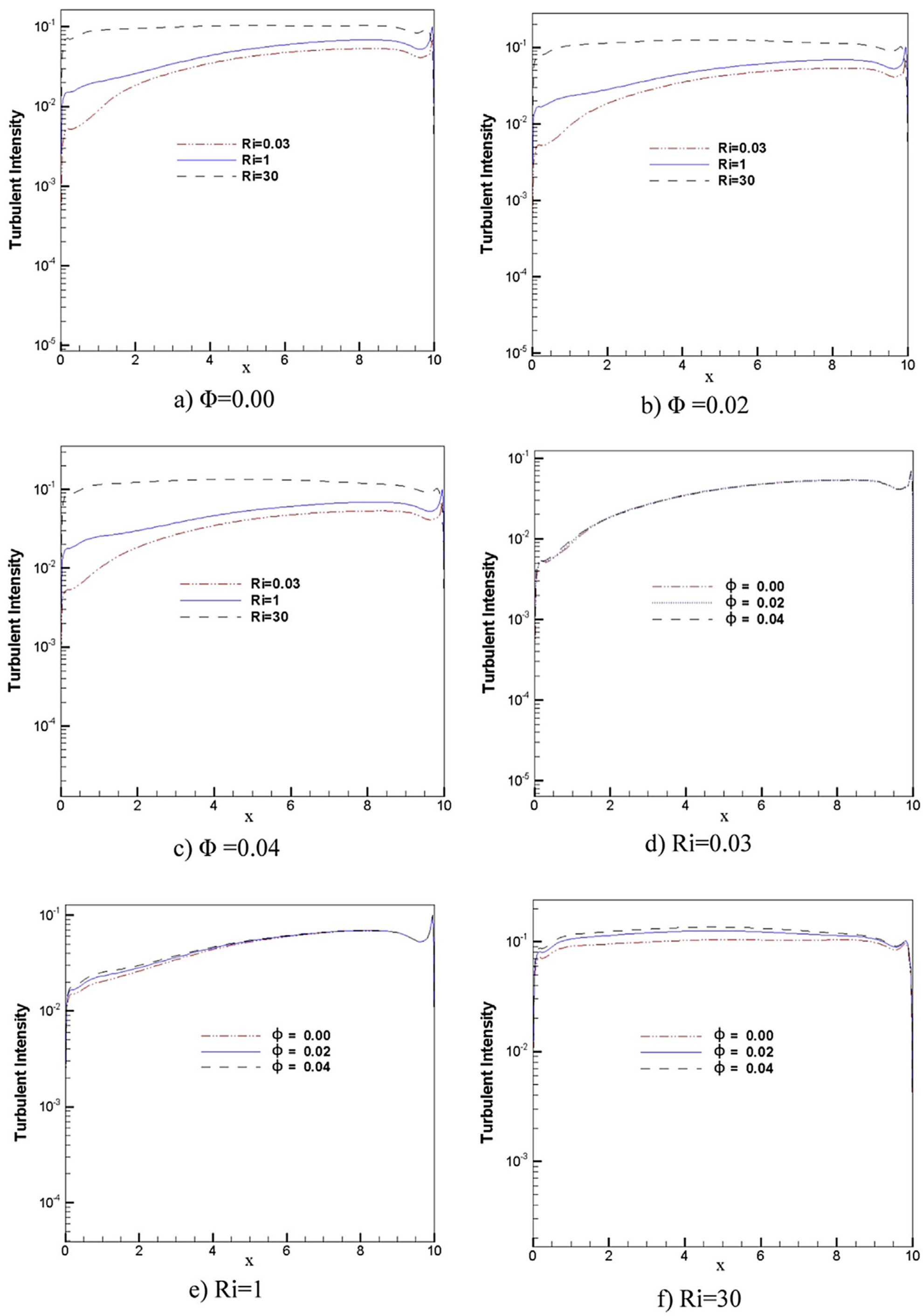

Fig. 9. Turbulence Intensity representation at $Y/H = 0.5$ for different Richardson numbers.

6. Results

The primary results for mixed convection within a rectangular cavity with a top moving wall are presented in this section. A pertinent dimensionless parameter here is the Richardson number, which varies from 0.03 to 30. The Richardson number is a measure of the ratio of natural convection to forced convection expressed as $Ri = Gr/Re^2$. When $Ri \to \infty$ or$Ri \to 0$, the dominant heat transfer mechanisms are free or forced convection, respectively [79]. The Grashof number is set at 10^5 for laminar flow and 10^{10} for turbulent flow. The volume fraction of nanoparticles ranges from 0.00 to 0.04. For calculating the dimensionless parameters, distances are normalized by the cavity length *W*, velocities are normalized by the lid velocity U_{lid}, pressure is normalized by $\rho_m U_{\text{lid}}^2$ and the temperature is normalized as $T - T_c/T_h - T_c$ [4].

6.1. Streamlines and isotherms

Figs. 5–8 illustrate the streamline and isotherm contours inside the cavity for different Richardson numbers and various nanoparticle volume fractions. In general, flow is generated by the moving upper wall. A clockwise primary (covering most of the area)

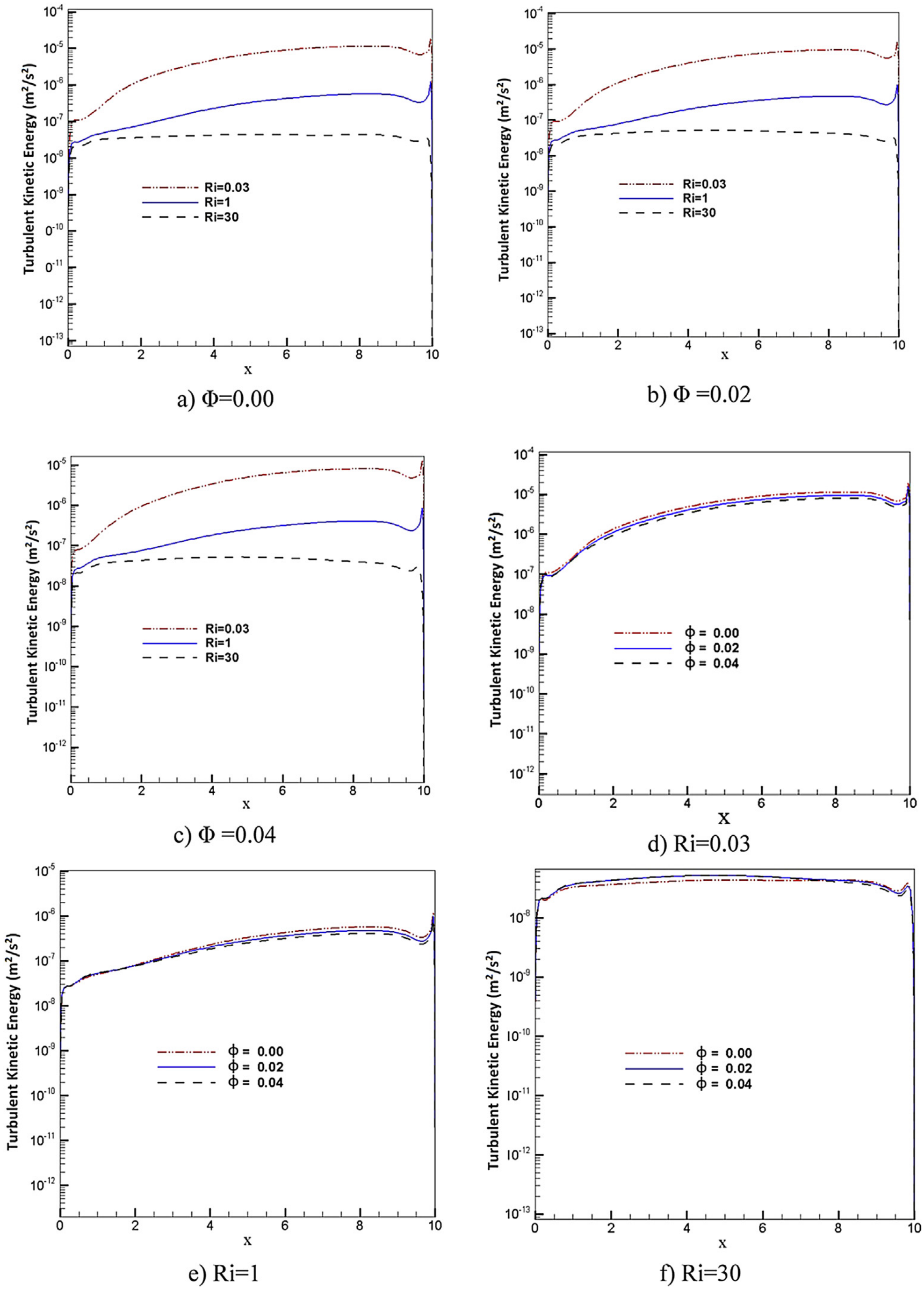

Fig. 10. Turbulence Kinetics Energy diagram at $Y/H = 0.5$ for different Richardson numbers.

vortex is formed inside the cavity due to the movement of the nanofluid near the upper wall. For laminar flow cases, Fig. 5 shows that for high values of *Ri*, the stream function does not change appreciably when the solid volume fractions changes.

When $Ri = 0.03$ (Figs. 5a–c) the flow field is shaped by a clockwise eddy next to the right wall; the shear-driven flow by the lid strongly affects the sidewall and moves downwards. However, if Ri increases and the solid volume fraction remains constant, the free convection inside the cavity enhances, causing the core of primary eddy to become smaller and slightly moves to left (Fig. 5d–i).

Fig. 7 shows that in the laminar flow case and for $Ri = 30$ (Fig. 7g–i), the entire cavity is in a thermally stratified state which is characterized by streamlines and isotherms that are almost parallel lines in the horizontal direction, except for the streamlines near the side walls. By increasing the shear force (increasing top wall velocity), the stratification disappears to some extent for Ri = 1 (Fig. 7d–f) and is completely distorted for $Ri = 0.03$ (Fig. 7a–c).

For the turbulent flow case shown in Fig. 6, however, as *Ri* increases the influence of the primary eddy diminishes markedly. At $Ri = 0.03$ (Fig.6a–c) the flow field is entirely controlled by the moving upper wall, and is also sensitive to magnitude of solid volume fraction. In this case, there is a stagnant region at the bottom left side of the cavity; the extent of this zone is reduced as the solid volume fraction increases.

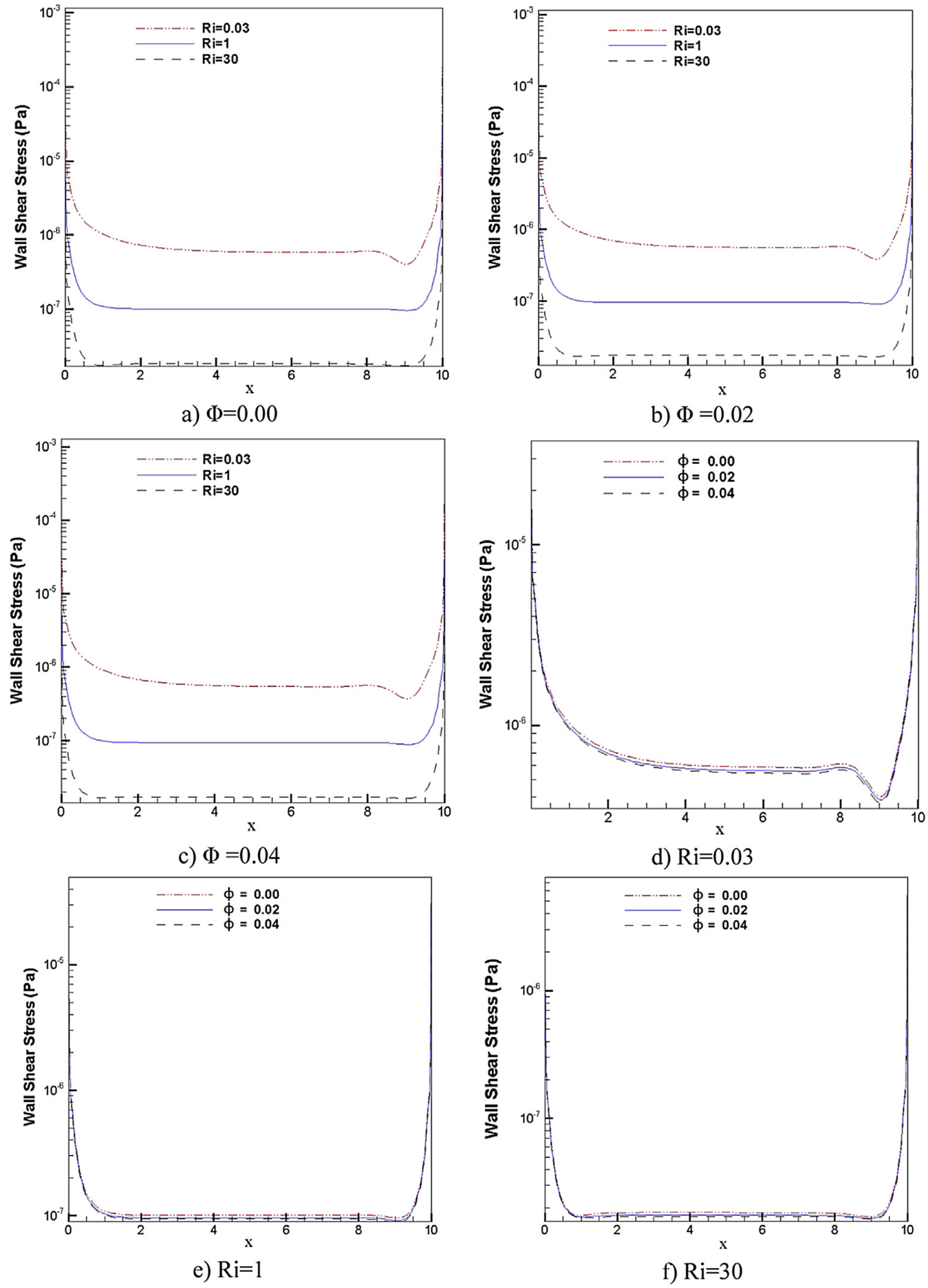

Fig. 11. Wall shear stress profiles for different solid volume fractions and Richardson numbers in the laminar regime.

In case of mixed convection ($Ri = 1$, Fig. 6d–f) where forced and free convection coexist, the stretching of the main eddy increases due to the cessation of free convection in the cavity with the enhanced nanofluid effective viscosity. As a result the peak value of the stream function decreases about 4 times compared with that for $Ri = 0.03$.

For the free convection with $Ri = 30$ (Fig. 6g–i) with the bottom wall heated, the large eddy becomes denser, especially near the top and bottom walls and the peak value of the stream function is about 3.5 times less than similar values for the mixed convection state.

Among all cases studied, the strongest recirculation region was observed for $\Phi = 0.04$ and $Ri = 0.03$, which corresponds to the highest heat transfer augmentation.

Furthermore, the isotherms for $Ri = 30$ shown in Fig. 8g–i demonstrate the appearance of a thin thermal boundary layer around the lower wall. Also in this state, the formation of a thin, hydrodynamic boundary layer in the direction of the moving top wall can be seen.

For the mixed convection at $Ri = 1$ (Fig. 8d–f) and forced convection at $Ri = 0.03$ (Fig. 8a–c), it can be seen that when the Richardson number decreases, the temperature close to the left

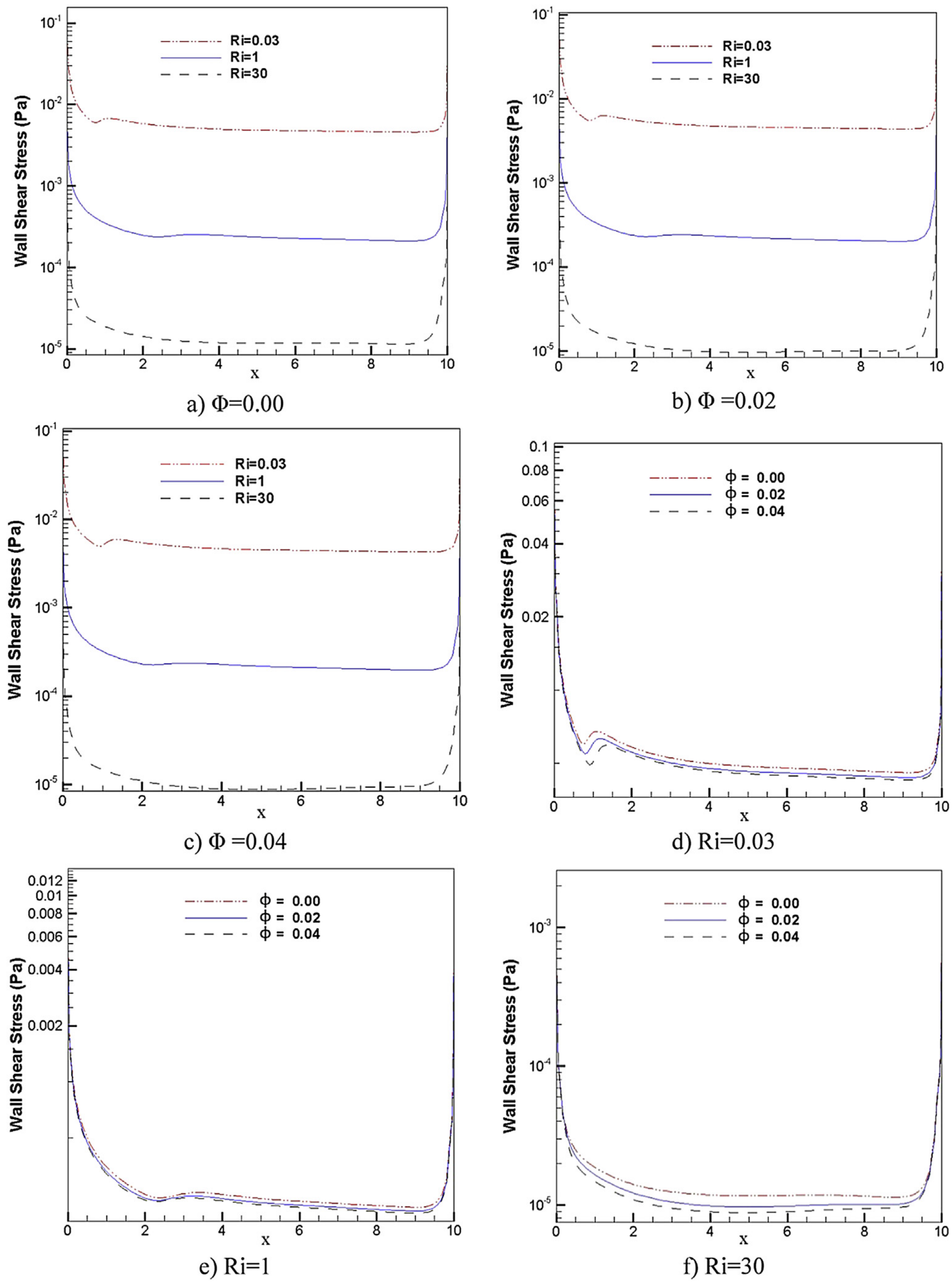

Fig. 12. Wall shear stress profiles for different solid volume fractions and Richardson numbers in turbulent flow regimes.

side of cavity remains roughly unchanged but the temperature variation near the right side of the cavity is noticeable.

6.2. Turbulence intensity

Turbulence intensity is defined as the ratio of root mean-square fluctuation velocity to the average flow velocity, that is:

$$\xi = \frac{u_{\rm rms}}{\overline{u}} = \frac{\left[\left(\overline{u'^2}\right)\right]^{\frac{1}{2}}}{\overline{u}} = \frac{\sqrt{\frac{2}{3}K}}{\sqrt{\overline{u}_x^2 + \overline{u}_y^2}} \tag{35}$$

Turbulence intensities are deemed small if they are below 1% and considered large if they are above 10%. Fig. 9 shows turbulence intensity profiles inside the cavity at mid-height. As can been seen from the figure, the magnitude of turbulence intensity inside cavity in all cases is low. This figure additionally shows that the minimum turbulence intensity value is zero and is located at the left and right walls and the maximum value occurs within the right wall's boundary layer. For a constant *Ri*, when the nanoparticle volume fraction increases, turbulence intensity remains nearly constant. In this case, the only exception happens for $Ri = 30$, where turbulent intensity for Φ=0.04 is slightly different than those for Φ=0.00 and Φ=0.02. For constant solid volume fraction, turbulence intensity is maximum when $Ri = 30$ and at a minimum value when $Ri = 0.03$. The reason is the presence of stagnant region near the left wall in the forced convection regime. For natural convection, however, one large, strong eddy occupies the entire cavity as seen in Fig. 6.

6.3. Turbulent kinetic energy

The model predictions for the turbulence kinetic energy profiles at mid-height are presented in Fig. 10. The calculated values indicate that for a constant *Ri*, the fluctuation kinetic energy roughly has a constant value, for different solid volume fractions. In all cases, the turbulence kinetic energy close to the left and right walls increases sharply. For constant values of solid volume fraction, Fig. 10 also shows that increasing *Ri*, the turbulence kinetic energy decreases. Averages of the highest and the lowest turbulence kinetic energies are 4×10^{-5} m^2 S^{-2} and 2×10^{-7} m^2 S^{-2} for $Ri = 0.03$ and $Ri = 30$ respectively.

6.4. Wall shear stress

Figs. 11 and 12 show the wall shear stress variations at the hot wall for the laminar and turbulent regimes. Clearly, for a constant *Ri*, the wall shear stress values remain roughly the same for different solid volume fractions below 0.04. This is more so for laminar flow regime compared to the turbulent flow regime. This is due to the fact that, even though an increase of nanoparticle solid volume fraction results in an increase in the mixture viscosity, nevertheless, for a constant *Re*, the velocity of the top moving wall decreases. For a constant solid volume fraction, the wall shear stress decreases as *Ri* increases. For laminar flow case, the

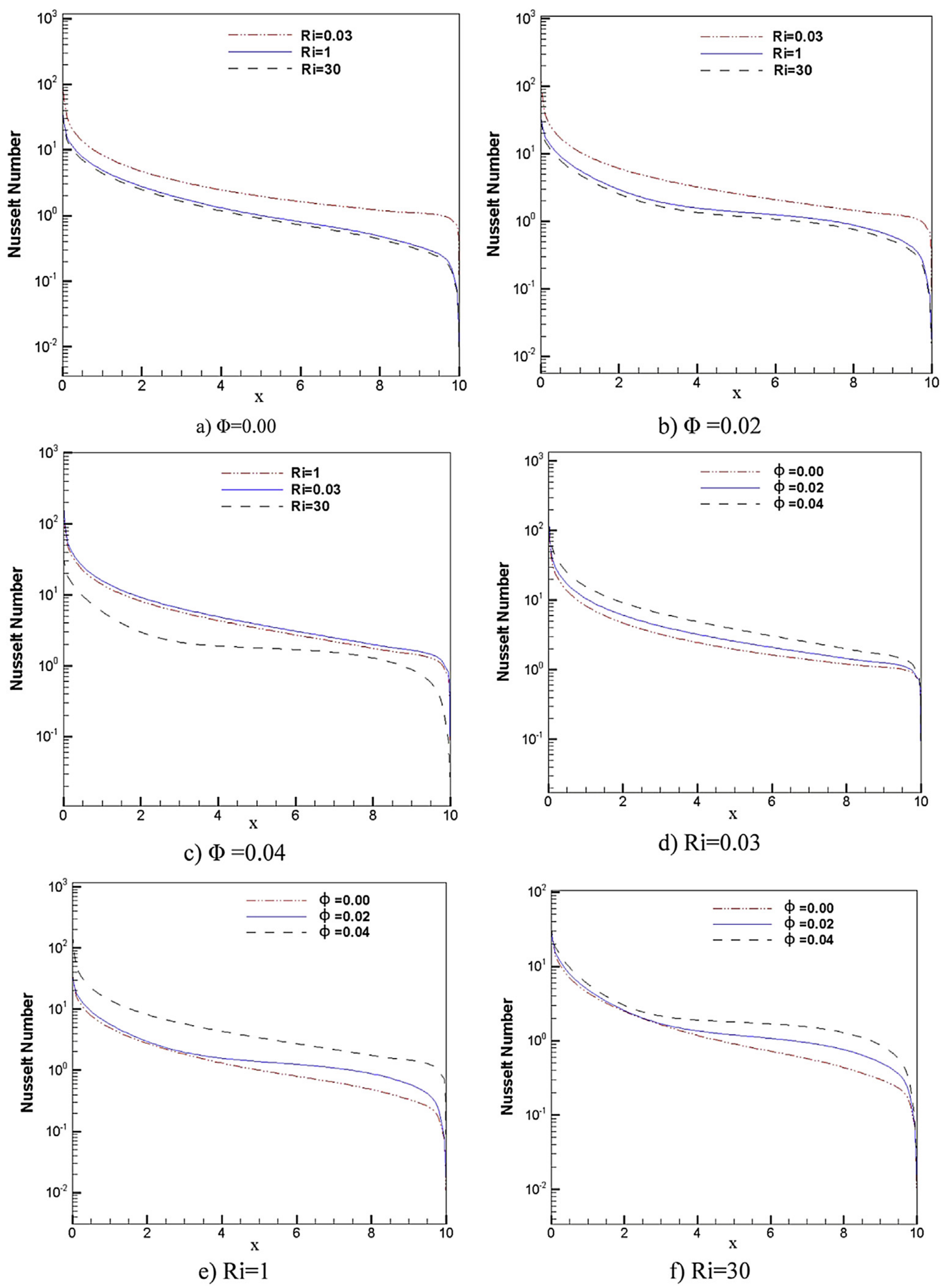

Fig. 13. Local Nusselt number profiles for different solid volume fractions and Richardson numbers in the laminar flow regime.

minimum wall shear stresses for $Ri = 0.03$ and $Ri = 30$ are around 5×10^{-6} Pa and 10^{-8} Pa respectively. For turbulent state, these values are around 4×10^{-2} for $Ri = 0.03$, 7×10^{-3} for $Ri = 30$ and 10^{-5} for $Ri = 30$.

6.5. Local Nusselt number

Figs. 13 and 14 illustrate the local Nusselt number distributions along the hot wall for various Richardson numbers and solid volume fractions for laminar and turbulent cases. For both situations, the Nusselt number is high at the left wall and decreases toward the right wall. The local Nusselt number plunges with a high gradient in the beginning and later continues to decrease with a much lower slope.

Fig. 14 illustrates three groups of *Ri* curves. The curves indicate that for the turbulent flow with a constant solid volume fraction, a reduction in the Richardson number leads to a significant enhancement in local Nusselt number. This enhancement is augmented by increasing the solid volume fraction. In Fig. 13, a similar trend is seen for the laminar flow regime. The effect of solid volume fraction, however, is not as prominent. It is generally clear from these figures that in all cases, the Nusselt number is highest

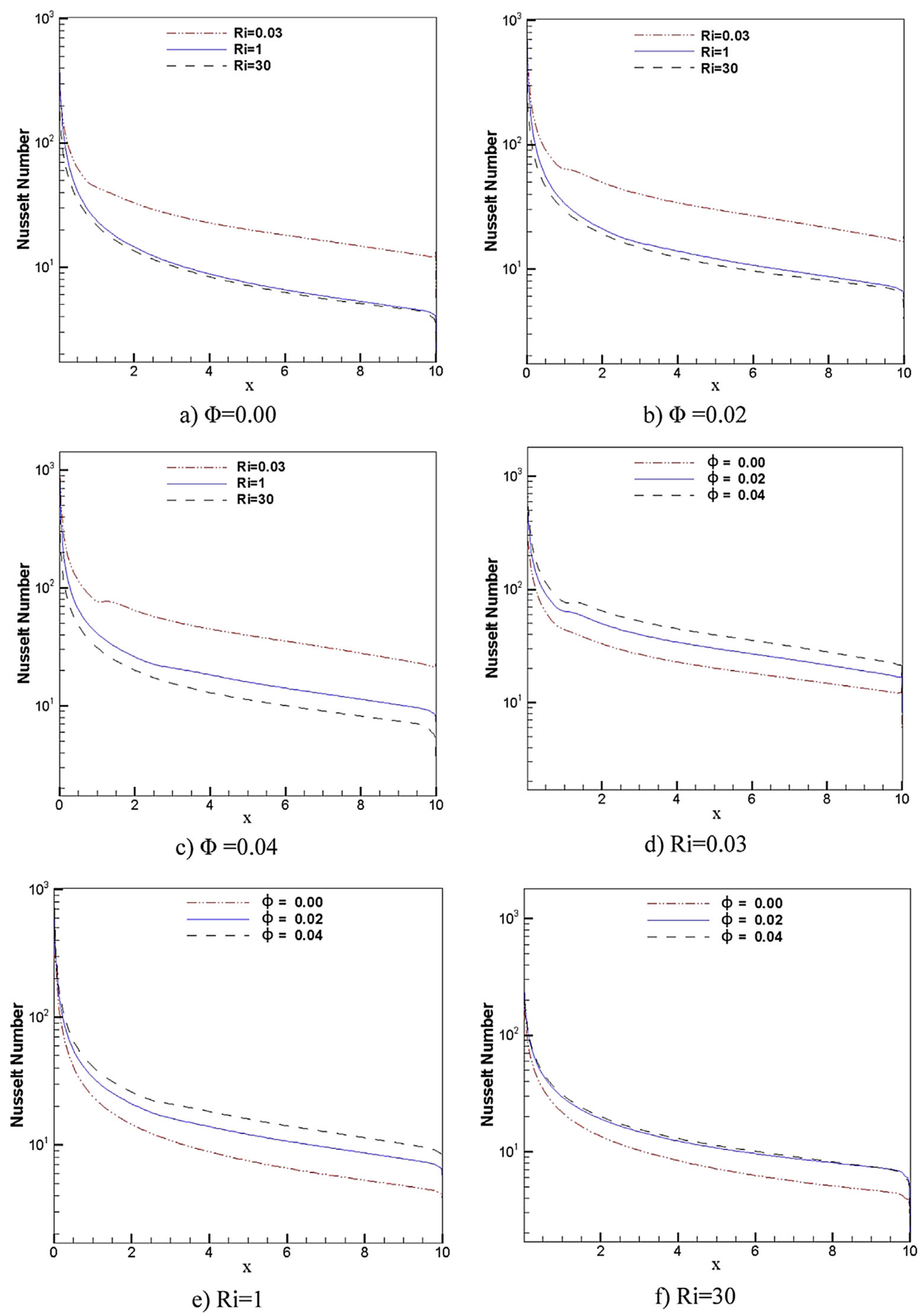

Fig. 14. Local Nusselt number profiles for different solid volume fractions and Richardson numbers in turbulent flow regime.

when forced convection is dominant and it is lowest when natural convection is dominant. As expected, the greater mixing in the turbulent flow regime enhances the heat transfer. Under similar conditions, increasing the volume fraction of nanoparticles leads to greater convective heat transfer and hence higher Nusselt numbers, since, at higher nanoparticle concentrations, the thermal conductivity increases. It is also clear that when forced convection is dominant, the Nusselt number is more sensitive to an increase in the solid volume fraction in comparison to a dominating natural convection condition.

6.6. Average Nusselt number

Variations of average Nusselt number versus Richardson number along the hot wall for different nanoparticle volume fractions are shown in Fig. 15. For all cases, the average Nusselt number is augmented as the volume fraction increases or when the Richardson number decreases. The highest Nusselt number was seen at 4% volume fraction and a Richardson number = 0.03. The heat transfer augmentation in this case is around 68.76% compared to pure water. The effect of nanoparticles on heat transfer enhancement in turbulent flow regime is more pronounced. The differences in Nusselt number for various solid volume fractions are also more significant when compared with those for the laminar flow regime.

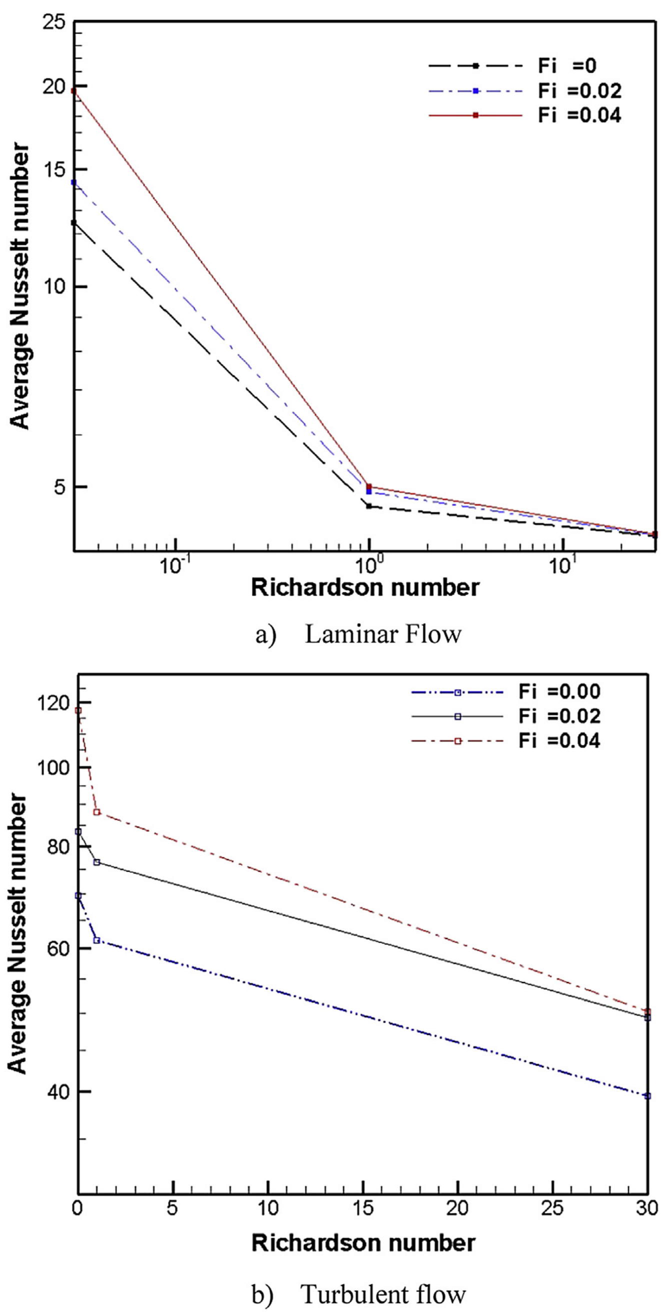

Fig. 15. Average Nusselt number representation for different solid volume fractions and Richardson numbers in laminar and turbulent flow regime.

7. Conclusions

A numerical study of laminar and turbulent mixed convection heat transfer of water-based/copper (Cu) nanofluid inside a cavity with AR = 0.1 was presented. The nanofluid was simulated as a two-phase mixture fluid and thermophysical properties of water in combination with nanoparticles were predicted utilizing the available models in literature. The presented mixture model included the effects of shear and Brownian motion of nanoparticles. Different solid volume fractions and Richardson numbers in laminar and turbulent regimes were considered. The flow and temperature fields as well as various parameters like, wall shear stress, turbulent intensity and local Nusselt number were evaluated.

The significant observations made on the mixed convection in a cavity are summarized as follows:

1) The Local Nusselt number, average Nusselt number and heat transfer coefficient of a nanofluid is augmented by increasing the volume fraction of nanoparticles.
2) The effects of the volume fraction on turbulent kinetic energy, turbulence intensity, skin friction and wall shear stress are insignificant.
3) At a low Richardson number ($Ri = 0.03$), a primary clockwise eddy forms inside the cavity. The vortex becomes smaller as the Richardson number increases.
4) For a constant Grashof number, the Nusselt number enhances with a decrease in the Richardson number.
5) Under similar conditions, higher Richardson numbers results in lower turbulence kinetics energies and wall shear stresses.

Acknowledgments

The authors gratefully acknowledge High Impact Research Grant UM.C/HIR/MOHE/ENG/23 and University of Malaya, Malaysia for support in conducting this research work.

References

[1] S.K. Das, S.U.S. Choi, W. Yu, T. Pradeep, Nanofluids: Science and Technology, Wiley Interscience, Hoboken, New Jersey, 2008.
[2] K. Khanafer, K. Vafai, Double-diffusive mixed convection in a lid-driven enclosure filled with a fluid-saturated porous medium, Numer. Heat Transf. Part A 42 (5) (2002) 465–486.
[3] S. Chung, K. Vafai, Vibration induced mixed convection in an open-ended obstructed cavity, Int. J. Heat Mass Transf. 53 (2010) 2703–2714.
[4] M.A.R. Sharif, Laminar mixed convection in shallow inclined driven cavities with hot moving lid on top and cooled from bottom, Appl. Therm. Eng. 27 (2007) 1036–1042.
[5] O. Manca, S. Nardini, K. Khanafer, K. Vafai, Effect of heated wall Position on mixed convection in a channel with an open cavity, Numer. Heat Transf. Part A 43 (3) (2003) 259–282.
[6] O. Manca, S. Nardini, K. Vafai, Experimental investigation of mixed convection in a channel with an open cavity, Exp. Heat Transf. 19 (1) (2006) 53–68.
[7] O. Manca, S. Nardini, K. Vafai, Experimental investigation of opposing mixed convection in a channel with an open cavity below, Exp. Heat Transf. 21 (2) (2008) 99–114.

[8] A. Marafie, K. Khanafer, B. Al-Azmi, K. Vafai, Non-darcian effects on the mixed convection heat transfer in a metallic porous block with a confined slot jet, Numer. Heat Transf. Part A 54 (7) (2008) 665–685.
[9] W. Shi, K. Vafai, Mixed convection in an obstructed open-ended cavity, Numer. Heat Transf. Part A 57 (10) (2010) 709–729.
[10] M. Muthtamilselvan, P. Kandaswamy, J. Lee, Heat transfer enhancement of copper–water nanofluids in a lid-driven enclosure, Commun. Nonlinear Sci. Num. Simul. 15 (2010) 1501–1510.
[11] E. Abu-Nada, A.J. Chamkha, Effect of nanofluid variable properties on natural convection in enclosures filled with a CuO–EG–water nanofluid, Int. J. Therm. Sci. 49 (2010) 2339–2352.
[12] A. Karimipour, M. Afrand, M.M. Bazofti, Periodic mixed convection of a nanofluid in a cavity with top lid sinusoidal motion, Int. J. Mech. Mater. Eng. 1 (1) (2010) 34–39.
[13] K.M. Khanafer, A.M. Al-Amiri, I. Pop, Numerical simulation of unsteady mixed convection in a driven cavity using an externally excited sliding lid, Eur. J. Mech. B Fluids 26 (2007) 669–687.
[14] H.F. Oztop, E. Abu-Nada, Numerical study of natural convection in partially heated rectangular enclosures filled with nanofluids, Int. J. Heat Fluid Flow 29 (2008) 1326–1336.
[15] B. Ghasemi, S.M. Aminossadati, Natural convection heat transfer in an inclined enclosure filled with a water–CuO nanofluid, Numer. Heat Transf. Part A 55 (2009) 807–823.
[16] J. Ravnik, L. Skerget, M. Hribersek, Analysis of three-dimensional natural convection of nanofluids by BEM, Eng. Anal. Bound. Elem. 34 (2010) 1018–1030.
[17] S.E.B. Maiga, C.T. Nguyen, N. Galanis, G. Roy, Heat transfer behaviors of nanofluids in a uniformly heated tube, Superlattices Microstruct. 35 (2004) 543–557.
[18] S.E.B. Maiga, S.J. Palm, C.T. Nguyen, G. Roy, N. Galanis, Heat transfer enhancement by using nanofluids in forced convection flows, Int. J. Heat Fluid Flow 26 (4) (2005) 530–546.
[19] S.E.B. Maiga, C.T. Nguyen, N. Galanis, G. Roy, T. Maré, M. Coqueux, Heat transfer enhancement in turbulent tube flow using Al_2O_3 nano-particle suspension, Int. J. Numer. Methods Heat Fluid Flow 16 (3) (2006) 275–292.
[20] V. Bianco, O. Manca, S. Nardini, Numerical simulation of water/Al_2O_3 nanofluid turbulent convection, Adv. Mech. Eng. (2010) 1–10.
[21] C.T. Nguyen, G. Laplante, M. Curyand, G. Simon, Experimental investigation of impinging jet heat transfer and erosion effect using Al_2O_3/water nanofluid, in: 6th IASME/WSEAS Int. Conf. Fluid Mech. Aerodyn. (FMA'08), Rhodes, Greece, 2008.
[22] K.Y. Leong, R. Saidur, S.N. Kazi, A.H. Mamun, Performance investigation of an automotive car radiator operated with nanofluid-based coolants (nanofluid as a coolant in a radiator), Appl. Therm. Eng. 30 (2010) 2685–2692.
[23] K.Y. Leong, R. Saidur, T.M.I. Mahlia, Y.H. Yau, Modeling of shell and tube heat recovery exchanger operated with nanofluid based coolants, Int. J. Heat Mass Transf. 55 (2012) 808–816.
[24] A. Ijam, R. Saidur, Nanofluids as a Coolant for Electronic Devices, Lap Lambert Academic Publishing, 2012.
[25] C. Truesdell, R.A. Toupin, The classical field theories, in: S. Flugge (Ed.), Handb. Phys, vol. III/I, Springer Verlag, Berlin, 1960.
[26] A.C. Eringen, J.D. Igram, A continuum theory of chemically reacting media-II, Int. J. Eng. Sci. 3 (1965) 147–212.
[27] D.S. Drumheller, A. Bedford, A thermodynamical theory for reacting immiscible mixtures, Arch. Ration. Mech. Anal 73 (1980) 257–284.
[28] G. Ahmadi, Mechanics of saturated granular materials, Int. J. Nonlinear Mech. 15 (1980) 251–262.
[29] G. Ahmadi, On mechanics of incompressible multiphase suspensions, Adv. Water Resour. 10 (1987) 32–43.
[30] G. Ahmadi, D. Ma, A thermodynamical formulation for dispersed multiphase turbulent flows, part I: basic theory, Int. J. Multiph. Flow 16 (1990) 323–340.
[31] S. Abu-Zaid, G. Ahmadi, A thermodynamically consistent rate-dependent model for turbulent two-phase flows, Int. J. Nonlinear Mech. 30 (1995) 509–529.
[32] G. Ahmadi, J. Cao, L. Schneider, A. Sadiki, A thermodynamic formulation for chemically active multiphase turbulent flows, Int. J. Eng. Sci. 44 (2006) 699–720.
[33] M. Shariat, A. Akbarinia, A. Hossein Nezhad, A. Behzadmehr, R. Laur, Numerical study of two phase laminar mixed convection nanofluid in elliptic ducts, Appl. Therm. Eng. 31 (2011) 2348–2359.
[34] S. Alikhani, A. Behzadmehr, M. Saffar-Avval, Numerical study of nanofluid mixed convection in a horizontal curved tube using two-phase approach, Heat Mass Transf. 47 (2011) 107–118.
[35] M. Izadi, A. Behzadmehr, D. Jalali-Vahida, Numerical study of developing laminar forced convection of a nanofluid in an annulus, Int. J. Therm. Sci. 48 (2009) 2119–2129.
[36] O. Ghaffari, A. Behzadmehr, H. Ajam, Turbulent mixed convection of a nanofluid in a horizontal curved tube using a two-phase approach, Int. Commun. Heat Mass Transf. 37 (2010) 1551–1558.
[37] R. Lotfi, Y. Saboohi, A.M. Rashidi, Numerical study of forced convective heat transfer of nanofluids: comparison of different approaches, Int. Commun. Heat Mass Transf. 37 (2010) 74–78.
[38] R. Mokhtari Moghari, A. Akbarinia, M. Shariat, F. Talebi, R. Laur, Two phase mixed convection Al_2O_3–water nanofluid flow in an annulus, Int. J. Multiph. Flow 37 (2011) 585–595.
[39] V. Bianco, S. Nardini, O. Manca, Enhancement of heat transfer and entropy generation analysis of nanofluids turbulent convection flow in square section tubes, Nanoscale Res. Lett. 6 (2011) 252.
[40] M. Akbari, N. Galanis, A. Behzadmehr, Comparative assessment of single and two-phase models for numerical studies of nanofluid turbulent forced convection, Int. J. Heat Fluid Flow 37 (2012) 136–146.
[41] M. Nuim Labib, Md. J. Nine, H. Afrianto, H. Chung, H. Jeong, Numerical investigation on effect of base fluids and hybrid nanofluid in forced convective heat transfer, Int. J. Therm. Sci. 71 (2013) 163–171.
[43] D. Choudhury, Introduction to the Renormalization Group Method and Turbulence Modeling, Fluent Inc. Tech, 1993. Memorandum TM-107.
[44] J.D. Posner, C.R. Buchanan, D. Dunn-Rankin, Measurement and prediction of indoor air flow in a model room, Energy Build. 35 (2003) 515–526.
[45] A. Guardo, M. Coussirat, M.A. Larrayoz, F. Recasens, E. Egusquiza, Influence of the turbulence model in CFD modeling of wall-to-fluid heat transfer in packed beds, Chem. Eng. Sci. 60 (6) (2005) 1733–1742.
[46] K. Mansour, M. Yahyazade, Effects of turbulence model in computational fluid dynamics of horizontal axis wind turbine aerodynamic, WSEAS Trans. Appl. Theor. Mech. 3 (6) (2011) 108–118.
[47] M.R. Safaei, Y. Maghmoumi, A. Karimipour, Numerical investigation of turbulence mixed convection heat transfer of water and drilling mud inside a square enclosure by finite volume method, in: 4th Int. Meet. Adv. Thermofluids, IMAT 2011; Melaka, Malaysia, 2011.
[48] B. Ghasemi, S.M. Aminossadati, Periodic natural convection in a nanofluid-filled enclosure with oscillating heat flux, Int. J. Therm. Sci. 49 (2010) 1–9.
[49] A. Ramiar, A.A. Ranjbar, S.F. Hosseinizadeh, Effect of axial conduction and variable properties on two dimensional conjugate heat transfer of Al_2O_3–EG/water mixture nanofluid in microchannel, J. Appl. Fluid Mech. 5 (3) (2012) 79–87.
[50] K. Khanafer, K. Vafai, A critical synthesis of thermophysical characteristics of nanofluids, Int. J. Heat Mass Transf. 54 (2011) 4410–4428.
[51] C.H. Chon, K.D. Kihm, S.P. Lee, S.U.S. Choi, Empirical correlation finding the role of temperature and particle size for nanofluid (Al_2O_3) thermal conductivity enhancement, J. Appl. Phys. 87 (15) (2005) 153107–153107-3.
[52] H.A. Mintsa, G. Roy, C.T. Nguyen, D. Doucet, New temperature dependent thermal conductivity data for water-based nanofluids, Int. J. Therm. Sci. 48 (2009) 363–371.
[53] N. Masoumi, N. Sohrabi, A. Behzadmehr, A new model for calculating the effective viscosity of nanofluids, J. Phys. D Appl. Phys. 42 (2009) 055501–055506.
[54] K. Khanafer, K. Vafai, M. Lightstone, Buoyancy-driven heat transfer enhancement in a two-dimensional enclosure utilizing nanofluids, Int. J. Heat Mass Transf. 46 (2003) 3639–3653.
[55] O. Abouali, G. Ahmadi, Computer simulations of natural convection of single phase nanofluids in simple enclosures: a critical review, Appl. Therm. Eng. 36 (2012) 1–13.
[56] B.E. Launder, D.B. Spalding, The numerical computation of turbulent flows, Comput. Methods Appl. Mech. Eng. 3 (1974) 269–289.
[57] E. Abedini, A. Behzadmehr, S.M.H. Sarvari, S.H. Mansouri, Numerical investigation of subcooled flow boiling of a nanofluid, Int. J. Therm. Sci. 64 (2013) 232–239.
[58] S.V. Patankar, Numerical Heat Transfer and Fluid Flow, Hemisphere, Washington, 1980.
[59] M.R. Safaei, H.R. Goshayshi, B. Saeedi Razavi, M. Goodarzi, Numerical investigation of laminar and turbulent mixed convection in a shallow water-filled enclosure by various turbulence methods, Sci. Res. Essays 6 (22) (2011) 4826–4838.
[60] M.R. Safaei, B. Rahmanian, M. Goodarzi, Numerical study of laminar mixed convection heat transfer of power-law non-Newtonian fluids in square enclosures by finite volume method, Int. J. Phys. Sci. 6 (33) (2011) 7456–7470.
[61] H.R. Goshayshi, M.R. Safaei, Y. Maghmoumi, Numerical simulation of unsteady turbulent and laminar mixed convection in rectangular enclosure with hot upper moving wall by finite volume method, in: 6th Int. Chem. Eng. Congr. Exhib. (Ichec 2009), Kish Island, Iran, 2009.
[62] S. Mirmasoumi, A. Behzadmehr, Effect of nanoparticles mean diameter on mixed convection heat transfer of a nanofluid in a horizontal tube, Int. J. Heat Fluid Flow 29 (2008) 557–566.
[63] M. Akbari, A. Behzadmehr, F. Shahraki, Fully developed mixed convection in horizontal and inclined tubes with uniform heat flux using nanofluid, Int. J. Heat Fluid Flow 29 (2008) 545–556.
[64] A. Karimipour, M. Afrand, M. Akbari, M.R. Safaei, Simulation of fluid flow and heat transfer in the inclined enclosure, in: Int. Conf. Fluid Dyn. Thermodyn. (ICFDT 2012). Zurich, Switzerland, 2012.
[65] F. Ampofo, T.G. Karayiannis, Experimental benchmark data for turbulent natural convection in an air filled square cavity, Int. J. Heat Mass Transf. 46 (2003) 3551–3572.
[66] S.H. Peng, L. Davidson, Large eddy simulation for turbulent buoyant flow in a confined cavity, Int. J. Heat Fluid Flow 22 (2001) 323–331.
[67] M. Omri, N. Galanis, Numerical analysis of turbulent buoyant flows in enclosures: influence of grid and boundary conditions, Int. J. Therm. Sci. 46 (2007) 727–738.
[68] K.J. Hsieh, F.S. Lien, Numerical modeling of buoyancy-driven turbulent flows enclosures, Int. J. Heat Fluid Flow 25 (2004) 659–670.

[69] A. Abdel Wahab, E.E. Khalil, Mathematical modeling of turbulent flows in furnaces, in: 6th Int. Energy Convers. Eng. Conf. (IECEC), Cleveland, Ohio, U.S.A., 2008, pp. 1239–1248.
[70] A.S. Yadav, J.L. Bhagoria, Heat transfer and fluid flow analysis of solar air heater: a review of CFD approach, Renew. Sustain. Energy Rev. 23 (2013) 60–79.
[71] C.M. Teixeira, Incorporating turbulence models into the Lattice–Boltzmann method, Int. J. Mod. Phys. C 09 (08) (1998) 1159–1175.
[72] K. Saha, S.N. Singh, V. Seshadri, S. Mukhopadhyay, Computational analysis on flow through transition s-diffusers: effect of inlet shape, J. Aircr. 44 (1) (2007) 187–193.
[73] K. Hanjalic, Advanced turbulence closure models: a view of current status and future prospects, Int. J. Heat Fluid Flow 15 (3) (1994) 178–203.
[74] O. Kaario, M. Larmi, F. Tanner, Relating integral length scale to turbulent time scale and comparing $k-\varepsilon$ and RNG $k-\varepsilon$ turbulence models in diesel combustion simulation, in: SAE 2002 World Congr. & Exh., Detroit, Michigan, United States, U.S.A, 2002, pp. 2002-01-1117.
[75] S.S. Vargheseand, S.H. Frankel, Numerical modeling of pulsatile turbulent flow in Stenotic Vessels, J. Biomech. Eng. 125 (2003) 445–460.
[76] M. Hidayat, A. Rasmuson, Numerical assessment of gas–solid flow in a U-bend, IchemE Trans. Part A Chem. Eng. Res. Des. 82 (A3) (2004) 332–343.
[77] S.M. El-Behery, M.H. Hamed, M.A. El-Kadi, K.A. Ibrahim, CFD prediction of air–solid flow in 180° curved duct, Powder Technol. 191 (2009) 130–142.
[78] T.B. Gatski, M.Y. Hussaini, J.L. Lumley, Simulation and Modeling of Turbulent Flows, Oxford University Press, New York, U.S.A., 1996.
[79] A. Bejan, Heat Transfer, John Wiley & Sons, New Jersey, 1993.